Liquid–liquid phase separation of type II diabetes-associated IAPP initiates hydrogelation and aggregation

Lior Pytowski[a], Chiu Fan Lee[b], Alex C. Foley[a], David J. Vaux[a,1,2], and Létitia Jean[a,1]

[a]Sir William Dunn School of Pathology, University of Oxford, OX1 3RE Oxford, United Kingdom; and [b]Department of Bioengineering, Imperial College London, South Kensington Campus, SW7 2AZ London, United Kingdom

Edited by David A. Weitz, Harvard University, Cambridge, MA, and approved March 31, 2020 (received for review September 26, 2019)

Amyloidoses (misfolded polypeptide accumulation) are among the most debilitating diseases our aging societies face. Amyloidogenesis can be catalyzed by hydrophobic–hydrophilic interfaces (e.g., air–water interface in vitro [AWI]). We recently demonstrated hydrogelation of the amyloidogenic type II diabetes-associated islet amyloid polypeptide (IAPP), a hydrophobic–hydrophilic interface-dependent process with complex kinetics. We demonstrate that human IAPP undergoes AWI-catalyzed liquid–liquid phase separation (LLPS), which initiates hydrogelation and aggregation. Insulin modulates these processes but does not prevent them. Using nonamyloidogenic rat IAPP, we show that, whereas LLPS does not require the amyloidogenic sequence, hydrogelation and aggregation do. Interestingly, both insulin and rat sequence delayed IAPP LLPS, which may reflect physiology. By developing an experimental setup and analysis tools, we show that, within the whole system (beyond the droplet stage), macroscopic interconnected aggregate clusters form, grow, fuse, and evolve via internal rearrangement, leading to overall hydrogelation. As the AWI-adsorbed gelled layer matures, its microviscosity increases. LLPS-driven aggregation may be a common amyloid feature and integral to pathology.

IAPP | liquid–liquid phase separation | hydrogelation | aggregation | insulin

Deposition of proteinaceous aggregates, amyloids, is the hallmark of many degenerative diseases (e.g., type 2 diabetes mellitus [TIID]) (1). Understanding the intricacy of amyloidogenesis is paramount to alleviate disease burden on human health. Deposition of misfolded human islet amyloid polypeptide (hIAPP), concomitantly with control loss of coexpressed insulin, has been implicated in the loss of pancreatic β-cells in TIID (2).

Amyloidogenesis is a nucleation-dependent polymerization with monomers adopting β-sheet structures, self-assembling into nuclei (energetically unfavorable, lag phase), and elongating nuclei until equilibrium is reached and fibril extension ceases (plateau) (3). Hydrophilic–hydrophobic interfaces (HHIs) promote amyloidogenesis due to adsorption of amphiphilic amyloidogenic polypeptides, spatially concentrating amyloid precursors and promoting β-sheet formation (4, 5). HHIs include membranes in vivo (nonpolar phospholipid fatty acid tails and aqueous environment or charged headgroups), and the air–water interface (AWI) in vitro (nonpolar gas and polar aqueous solution). The AWI is reproducible and homogeneous, allowing dissection of amyloid interfacial behavior without being hindered by phospholipid complexity. We previously demonstrated that it provides a good model for dissecting HHI-driven amyloidogenesis (4, 6, 7). Such studies can pave the way for investigations using more physiological HHIs (e.g., biological membranes). Amyloid adsorption and aggregation on cellular membrane leads to membrane damage and represents an important cause of amyloid toxicity (8, 9). In TIID, increase in β-cell membrane permeability occurs concomitantly with hIAPP interacting with membranes (2).

Amyloids can undergo liquid–liquid phase separation (LLPS) and/or gelation (6, 10, 11). LLPS plays a crucial role during formation and maintenance of cellular membraneless organelles, but is also linked to pathology via increased irreversible hydrogelation through amyloid-like fibrillization interfering with normal cellular functions (10, 12, 13). We previously demonstrated, by rheology, hIAPP hydrogelation in the bulk and at the AWI, via a three-dimensional (3D) supramolecular fibrillar network, which was promoted by phospholipids (6). Two distinct kinetic regimes, collapsed to one in D_2O, led to hIAPP hydrogelation, suggesting the existence of multiple gelation pathways. We hypothesized that the kinetic variation in H_2O may result from LLPS.

In this study, we first show that hIAPP spontaneously underwent AWI-catalyzed LLPS without added triggers. The initial liquid hIAPP droplets matured into a hydrogel state, leading to fibrillar aggregation at the droplet surface. LLPS was independent of hIAPP amyloidogenic sequence as nonamyloidogenic rat IAPP (rIAPP) also underwent LLPS, whereas hydrogelation and aggregation were dependent. Moreover, we demonstrate that insulin modulated hIAPP LLPS, hydrogelation, and aggregation, but did not fully prevent them. To follow the evolution of the whole system, beyond the droplet stage, we designed an experimental setup, using several reporter molecules. We show that the whole system transitioned between liquid and hydrogel states with homogeneous kinetics in D_2O. We also developed analysis tools to demonstrate that, clusters of interconnected aggregates formed, moved coordinately in local flow fields, grew, and fused

Significance

Deposition of some aggregated and misfolded polypeptides (amyloids) is the hallmark of many degenerative diseases. Amyloid assembly is slow, unfavorable, and still poorly understood. Here, we show that liquid–liquid demixing (like oil forming droplets in water) of type II diabetes IAPP amyloid precursors is not dependent on the human amyloidogenic sequence and leads to the formation of a water-filled gel within phase-separated droplets. Both processes then trigger pathological aggregation at the droplet surface, which is modulated by insulin. This localized aggregation propagates to interconnect droplets, leading to a macroscopic meshwork formation with increased local viscosity, eventually percolating the whole system. These processes may be at the heart of the pathology of type II diabetes.

Author contributions: D.J.V. and L.J. designed research; L.P., A.C.F., and L.J. performed research; C.F.L. and D.J.V. contributed new reagents/analytic tools; L.P., C.F.L., D.J.V., and L.J. analyzed data; and L.J. wrote the paper.

The authors declare no competing interest.

This article is a PNAS Direct Submission.

[1]D.J.V. and L.J. contributed equally to this work.

[2]To whom correspondence may be addressed. Email: david.vaux@path.ox.ac.uk.

This article contains supporting information online at https://www.pnas.org/lookup/suppl/doi:10.1073/pnas.1916716117/-/DCSupplemental.

First published May 15, 2020.

together. Finally, we used a boron–dipyrrin (BODIPY)-derived molecular rotor to show an in situ increase in microviscosity as the AWI gelled layer matured, with the gel being more viscous and homogeneous in D_2O. These findings lend insights into the role of LLPS and hydrogelation during amyloidogenesis, and their consequences could be critical for cellular functions.

Results

Biotinyl hIAPP, an Assembly Reporter. To determine whether hIAPP undergoes LLPS, which could explain the multiple IAPP hydrogelation pathways seen previously, we needed an assembly reporter (6). We tested biotinyl IAPP (bIAPP) by "spiking" nonlabeled hIAPP reactions. As amyloid precursor modifications can interfere with assembly, we assessed whether the N-terminal biotinylation affected fibrillization by following fluorescence emission changes (from 445 to 482 nm) of the amyloid dye, thioflavin T (ThT) (14). We used avidin-Texas red (TR) instead of avidin-fluorescein, as fluorescein emission would interfere with that of ThT. For the microscopy (below), both avidin-fluorescein (e.g., see Fig. 2*B*) and avidin-TR (e.g., see Fig. 2*G*) were used and did not affect assembly. Above spike ratios of 1:9, bIAPP abolished fibrillization. At 1:9, bIAPP affected all kinetic parameters, increasing lag phase (1.3-fold), and decreasing elongation rate (2.3-fold) and plateau height (1.5-fold) (Fig. 1*A*). Subsequently, transmission electron microscopy (TEM) confirmed that bIAPP incorporated into mixed bIAPP–hIAPP fibrillar material. Fibrils could not contain bIAPP alone due to steric inhibition of fibrillization, and fibrils should not be "fully covered" with gold particles as the ratio is 1bIAPP:9hIAPP. Gold particles only associated with fibrils or peptide material from bIAPP-containing reactions. The infrequent gold particles found in hIAPP-only reactions were not associated with peptide material (empty white ring surrounds gold particle) (Fig. 1*B*).

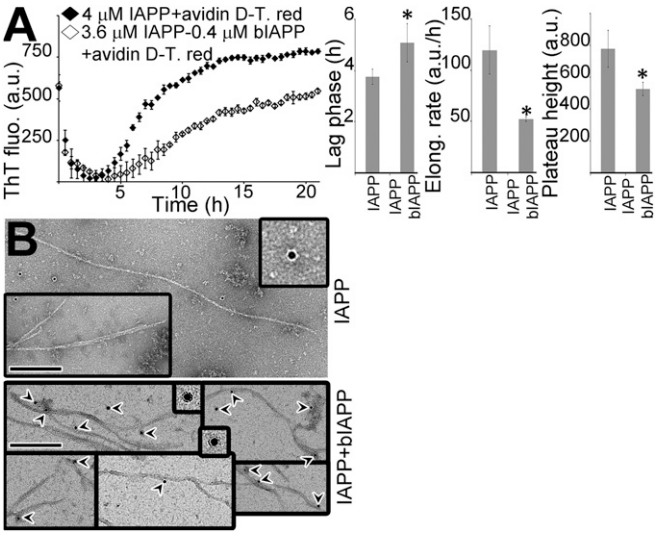

Fig. 1. bIAPP, an assembly reporter. (*A*) bIAPP delays fibrillization. A total of 4 μM hIAPP, or 3.6 μM hIAPP-0.4 μM bIAPP, was incubated with 0.08 μM avidin D TR and 32 μM ThT. ThT fluorescence changes were monitored with lag phase, elongation rate, and plateau height depicted. $*P < 0.03$ when compared to hIAPP alone. a.u., arbitrary units. $n = 3$, error bars ± SEM. (*B*) bIAPP incorporates into mixed bIAPP-hIAPP fibrils. Plateaued reactions were adsorbed onto grids, labeled with streptavidin 10 nm gold particles, and negatively stained. (Scale bars, 200 nm.) Arrowheads show gold particles associated with peptide material. (*Insets*) Gold particle zoom up.

hIAPP Undergoes LLPS into Droplets with Liquid-Like Properties. LLPS is characterized by liquid droplets phase separating from the aqueous environment, droplet sphericity due to surface tension, rapid droplet internal molecular rearrangement, and droplet fusion. Using time-lapse microscopy of reactions, without any added trigger (e.g., macromolecular crowding), we show that hIAPP underwent LLPS, with the time for onset being concentration dependent (*SI Appendix*, Fig. S1). To facilitate further experimentation, we chose a concentration of 129 μM. hIAPP spontaneously assembled into round micrometer-sized droplets, with their number and size increasing over time (LLPS onset ∼8.4 min, and individual droplet size increasing ∼15 min) (Fig. 2*A* and Movie S1). The droplets contained hIAPP as thioflavin S (ThS) and bIAPP-avidin D fluorescein labeled them (Fig. 2 *B*, *Left*). No droplet formation was observed for reporters alone (Fig. 2 *B*, *Right*). Droplet calculated sphericity was near that of perfect spheres (∼0.97) (Fig. 2*C*). Droplets underwent fusion, with relaxation into larger droplets within a few seconds, consistent with liquid-like properties (Fig. 2*D* and Movie S2). To assess droplet internal molecular mixing, we performed fluorescence recovery after photobleaching (FRAP), bleaching only part of the droplet (Fig. 2*E*). Early after LLPS onset, ThS fluorescence rapidly redistributed to the bleached droplet area (2 and 22 min, ∼96.5 to 70.5% mobility and 3.5 to 29.5% immobility, respectively). Thus, hIAPP molecules freely diffused within droplets, showing droplet liquid-like properties.

LLPS Precedes Droplet Hydrogelation. We then assessed whether the droplets transitioned to a gel-like state. During gelation, viscosity increase leads to a decrease in molecular diffusion rate. As the reaction progressed, ThS fluorescence redistribution to the bleached droplet area progressively decreased (Fig. 2*E*). Within droplets, hIAPP molecules went from being highly mobile (see above), to moderately mobile (52 min, ∼35.3% mobility), and to highly immobile (62 and 72 min, 77.5 to 89% immobility, respectively). Therefore, the droplets transitioned to a solid-like state, i.e., maturation into a hydrogel. We then performed FRAP on whole droplets (Fig. 2*F*). At 2 min post-LLPS, only 21.3% of molecules were mobile, showing that molecular exchange between droplets and solution was almost lost. The mobility decreased further to 4.1% at 72 min. Altogether, our FRAP experiments suggest that once formed droplets acquired rapidly hIAPP molecules, then became quickly "impermeable" to the surrounding solution (e.g., solid-like coat formation at the droplet surface). This preceded molecular rearrangement within droplets to finally form uniform solid-like droplets.

hIAPP LLPS Is AWI Catalyzed. We previously showed that amyloidogenesis and hydrogelation are catalyzed by HHIs, e.g., AWI (4, 6, 7). hIAPP spontaneous LLPS first occurred at the sample outer edge, i.e., the AWI (Fig. 2*G* and Movie S1). Over time, LLPS at the AWI "grew" to saturate the AWI with assemblies before propagating into the bulk. Although ThS and bIAPP labeling mostly overlapped, they also individually labeled discrete areas (Fig. 2 *G*, *Bottom*). Moreover, because of surface tension effect due to progressive hIAPP adsorption to the AWI, the reaction drop became flatter with the angle between coverslip and drop edge becoming smaller (z dimension became smaller). ThS and bIAPP distribution at the AWI and bulk also varied over time (Movie S3 and Fig. 3*A*). At the LLPS onset, most of the strong ThS labeling was at the AWI (e.g., 8 and 12.3 min). At later time points, the strong ThS labeling first surrounded the "big" droplets at the AWI (e.g., 23.3 min), before spreading along the AWI (e.g., 39.2 and 42.8 min) and then into the bulk (e.g., 48 min). In contrast, bIAPP labeling appeared mostly within and on the droplet surface all across the field of view. Both reporter intensity within droplets increased up to 20 min, before that of ThS plateauing, and that of bIAPP progressively decreasing (Fig. 3 *A*, *Bottom Right*). This suggests that, once gained, ThS labeling was not diluted from within droplets. These

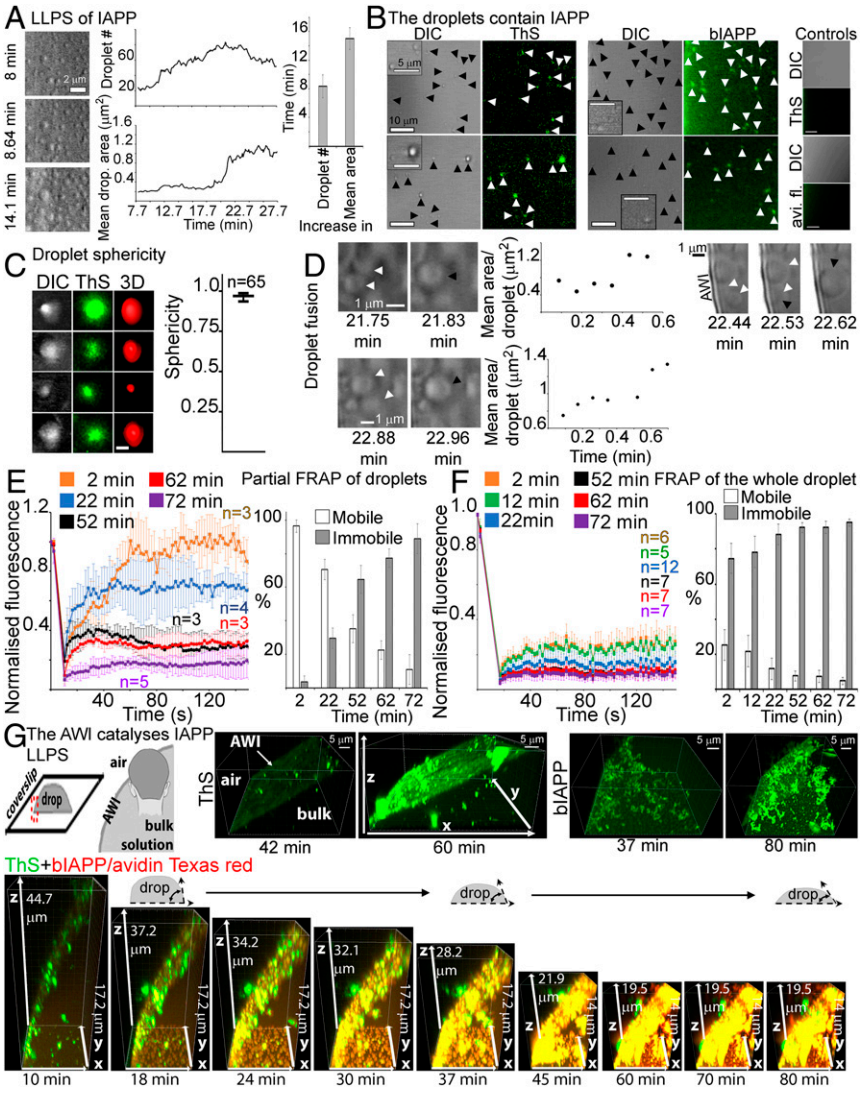

Fig. 2. hIAPP undergoes LLPS, with droplets transitioning between a liquid and gel-like state, and further maturing into an amyloid aggregated state. (*A*) Droplet accumulation and size increase over time (*Left*, Movie S1). Timing of droplet appearance (LLPS onset) and size increase (droplet fusion) (plots: representative of three independent replicates; bar graph: $n = 3$). (*B*) Phase-separated droplets contain hIAPP as they label with ThS or bIAPP-avidin fluorescein. *Insets*: droplet zoom up. No LLPS was observed for ThS or avidin fluorescein (avi. fl.) alone. (*C*) hIAPP droplets are spherical. DIC, ThS labeled and rendered droplet surface (*Left*). Droplet sphericity (~0.97) (*Right*). (*D*) Droplets fuse (white arrowheads) and relax into larger droplets (black arrowhead) (Movie S2), also indicated by droplet size growth (plots). (*E*) hIAPP molecule rearrangement within droplets at different times after LLPS onset. ThS-hIAPP fluorescence intensity recovery within a droplet bleached region, and fraction of mobile/immobile molecules. n = droplet number analyzed from at least three independent replicates. (*F*) hIAPP molecule exchange between droplets and bulk at different times after LLPS onset. ThS-hIAPP fluorescence intensity recovery within whole bleached droplets, and fraction of mobile/immobile molecules. n = droplet number analyzed from at least three independent replicates. (*G*) The AWI catalyses LLPS and aggregate size increases over time. (*Left Top*) A hIAPP reaction drop was pipetted on a MatTek dish, z stacks collected over time, and 3D reconstruction shows a side view of the AWI with bulk beneath. Three-dimensional projection of a hIAPP reaction with ThS (*Middle Top*), bIAPP-avidin fluorescein (*Right Top*), and ThS/bIAPP-avidin TR (*Bottom*). All images from one experiment have identical display settings.

experiments demonstrate that early in an hIAPP reaction, LLPS is catalyzed by the AWI, before propagating into the bulk.

Labeling Distribution within, on, and around Droplets Varies over Time. Reporter distribution can delineate different assembly stages since bIAPP should incorporate within all stages, whereas ThS would detect assemblies beyond nuclei (fluorescence at 480 nm only when intercalated into stacked β-sheets). Therefore, we examined z slices of ThS-bIAPP avidin-TR reactions, which encompassed droplets below and above their focal plane. At early time points, when droplet intramolecular mobility was still high, the droplet surface acquired the earliest and strongest labeling overall (Fig. 3*B* and Movie S3). At 18 min, the droplet surface mostly labeled with bIAPP. At 30 min, the droplet surface and interior started to have more ThS labeling, labeling that had increased at 45 min. Over time, the fluorophore overlap also increased, and so did the labeling within droplets (significantly for bIAPP, 18 to 30 min) (Fig. 3 *B*, *Middle* and *Right*). Although ThS and bIAPP mostly colocalized, they also labeled separate discrete areas. For all time points, 92 to 100% of ThS labeling overlapped with that of bIAPP, whereas bIAPP labeling overlap with that of ThS increased over time (from 62 to 88%). Small aggregates were also observed, with their size increasing over time (arrowhead). We confirmed, within the whole z stack, that droplet interiors contained hIAPP (Fig. 3*C*). ThS labeling significantly increased (up to 45 min) before decreasing (45 to 60 min) to a plateau (>60 min). bIAPP-avidin-TR intensity followed a similar increase (up to 45 min), but first plateaued (45 to 70 min) before decreasing (beyond 80 min). These experiments show that the overall labeling, both droplet surface and interior, varied over time, and the two reporters labeled discrete separate areas.

hIAPP Droplet Maturation Leads to Aggregate Formation and Creation of an Interconnected Fibrillar Network. We then investigated whether the hIAPP gel-like droplets can further "mature" into an irreversible amyloid aggregated state. Beyond 60 min (when droplet internal molecular immobility was high, Fig. 2*E*), aggregates of a few micrometers labeled with ThS and bIAPP-avidin-TR had formed (Fig. 4 *A*, *Left* and zoom up). These were clearly visible on the differential interference contrast (DIC) images, and consisted of a strongly double-labeled core from which more weakly double-labeled fibrils projected outward. For all time points, ThS labeling completely overlapped with that of bIAPP (99.6 to 100%), whereas bIAPP labeling only partially overlapped with that of ThS (49 to 66%) (Fig. 4 *A*, *Bottom Right*). Fibrils and fibrillar aggregates (<1 μm) also developed on the droplet surface, growing and radiating outward (Fig. 4 *B*, *Top*). The droplet interior and small aggregates were strongly ThS and bIAPP positive, whereas fibrils had a weaker labeling. Fibrillar projections, from the core of a micrometer-size aggregate, extended to create a fibrillar

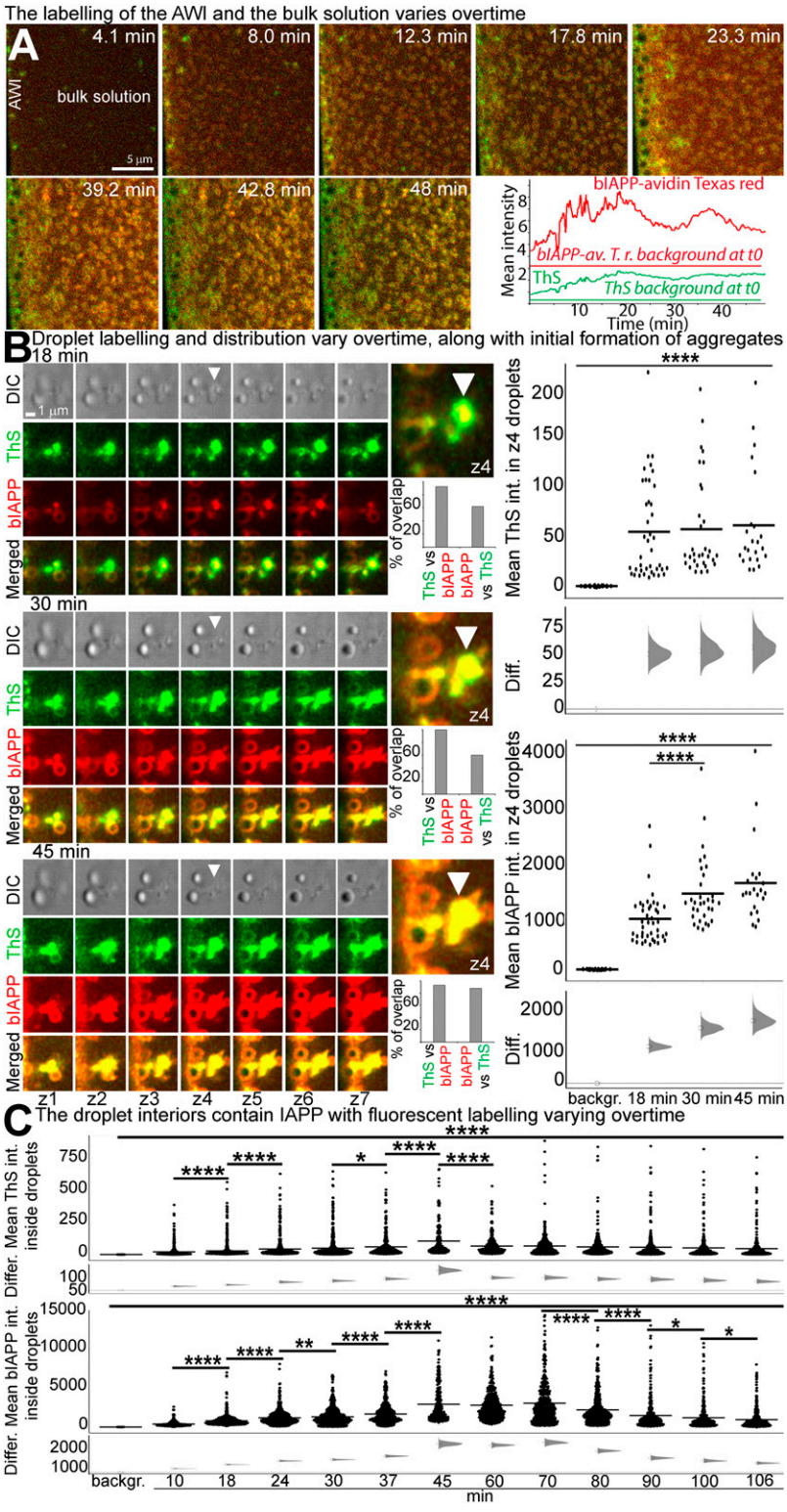

Fig. 3. The labeling distribution varies over time. (*A*) AWI and bulk labeling variation (Movie S3). Merged images of ThS/bIAPP-avidin-TR labeling over time. Mean intensity of ThS or bIAPP-avidin-TR within droplets (*Bottom Right*). Background fluorescence (horizontal lines): bulk fluorescence at t0. (*B*) Droplet labeling variation and initial aggregation. Consecutive z slices from a reaction at 18, 30, and 45 min (*Left*). z4 zoom up: 2 droplets in a similar focal plane (*Top Middle*). All images have identical display settings. White arrowhead: small aggregate. Overlap percentage between the two fluorophores within z4 (*Bottom Middle*). Mean intensity (int.) of ThS or bIAPP-avidin-TR within droplets (*Top Right*). Background fluorescence (backgr.): bulk fluorescence at 10 min. $^{****}P < 0.007$. Difference (Diff.) between mean values, i.e., "effect size," was determined relative to background fluorescence (*Bottom Right*). Circle: mean, black line: 95% confidence interval around the difference, derived from the mean bootstrap distribution. (*C*) Droplet interiors contain hIAPP, with labeling initially increasing before plateauing and decreasing. Mean intensity of ThS or bIAPP-avidin-TR within droplets, and difference between mean values quantified over time from Fig. 2*G* double-labeled z stacks. $^{*}P < 0.05$, $^{**}P < 0.03$, $^{****}P < 0.007$.

network connecting all droplets together (Fig. 4*B*). The aggregates were clearly fibrillar, as individual fibril bundles were visible. ThS positivity suggests the amyloid stacked β-sheet nature of aggregates (*Discussion*). ThS positivity of phosphorylated tau441 aggregates forming from the droplet surfaces was also previously observed (15). After 150 min, the fibrillar aggregates formed at the droplet surface became larger (some >10 µm) with longer fibrils extending from their core (Fig. 4*C*). The fibrils not only connected droplets together but also aggregates together. The fibrillar nature of the droplet interior, of projections from the droplet surface and of the meshwork connecting droplets was confirmed by TEM (Fig. 4*D*). At 90 min, when droplet hydrogelation should be complete, a mixture of droplets either free (*Left* panel showing three droplets) or embedded within a fibrillar meshwork (*Right* panel) was observed. The droplet interior contained fibrils (black arrowhead), fibrils grew from the droplet

surface (black-white arrowhead), and also fibrils extended across the boundary from within the droplet to outside (white arrowhead). At 180 min, droplets were fully embedded within a fibrillar meshwork (*Left* panel showing eight droplets). The droplet interior contained various amounts of fibrils; fibrils covered the droplet surface from which they projected outward to interconnect droplets together (*Right Bottom*). Thus, hIAPP initially undergoes LLPS, and over time, the droplets mature into a hydrogel due to fibrillization within droplets, preventing further droplet fusion and triggering fibrillar aggregation from the droplet surface. The aggregates then form an interconnected fibrillar network.

LLPS Does Not Require hIAPP Amyloidogenic Sequence, but Droplet Hydrogelation and Aggregation Do. We investigated LLPS dependency on the amyloidogenic sequence by using nonfibrillogenic rIAPP. Five out of six residue substitutions in rIAPP occur in the amyloidogenic region, three being prolines, a β-sheet breaker. One hundred twenty nine μM rIAPP-12.89 μM biotinyl rIAPP (brIAPP) assembled into brIAPP-labeled droplets (LLPS onset ∼25.1 min, ∼3-fold slower than hIAPP), which first appeared at the AWI before propagating into the bulk, and their number and size increased over time (Fig. 5 *A*, *B*, and *G* and Movie S4). Droplets possessed liquid-like property as they underwent rapid fusion and relaxation into larger droplets, and rIAPP molecules freely diffused within droplets (Fig. 5 *C* and *D*). Up to ∼50 min post-LLPS, rIAPP molecular diffusion within droplets was similar to that of hIAPP (∼35 to 45% mobility). However, rIAPP droplet hydrogelation (∼80% molecular immobility) was ∼4-fold slower than that of hIAPP (255 and 62 min, respectively) (Fig. 5 *D* and *G*). FRAP of whole droplets showed that rIAPP molecular exchange between droplets and solution was high (Fig. 5*E*). Impermeable coat formation around droplets was delayed by 130-fold, 260 min for rIAPP and 2 min for hIAPP (Fig. 5 *E* and *G*). As reactions evolved, brIAPP labeling spanned a wider area of the AWI, within and around droplets (Fig. 5*F*). However, even at 240 min, rIAPP droplets never matured into aggregates (hIAPP aggregation started ∼60 min). These experiments demonstrate that LLPS is independent of hIAPP amyloidogenic sequence, although it accelerates it. However, droplet hydrogelation, solid-like coat formation at the droplet surface in a physiological time frame, and maturation into aggregates clearly are dependent on the presence of the aggregating sequence.

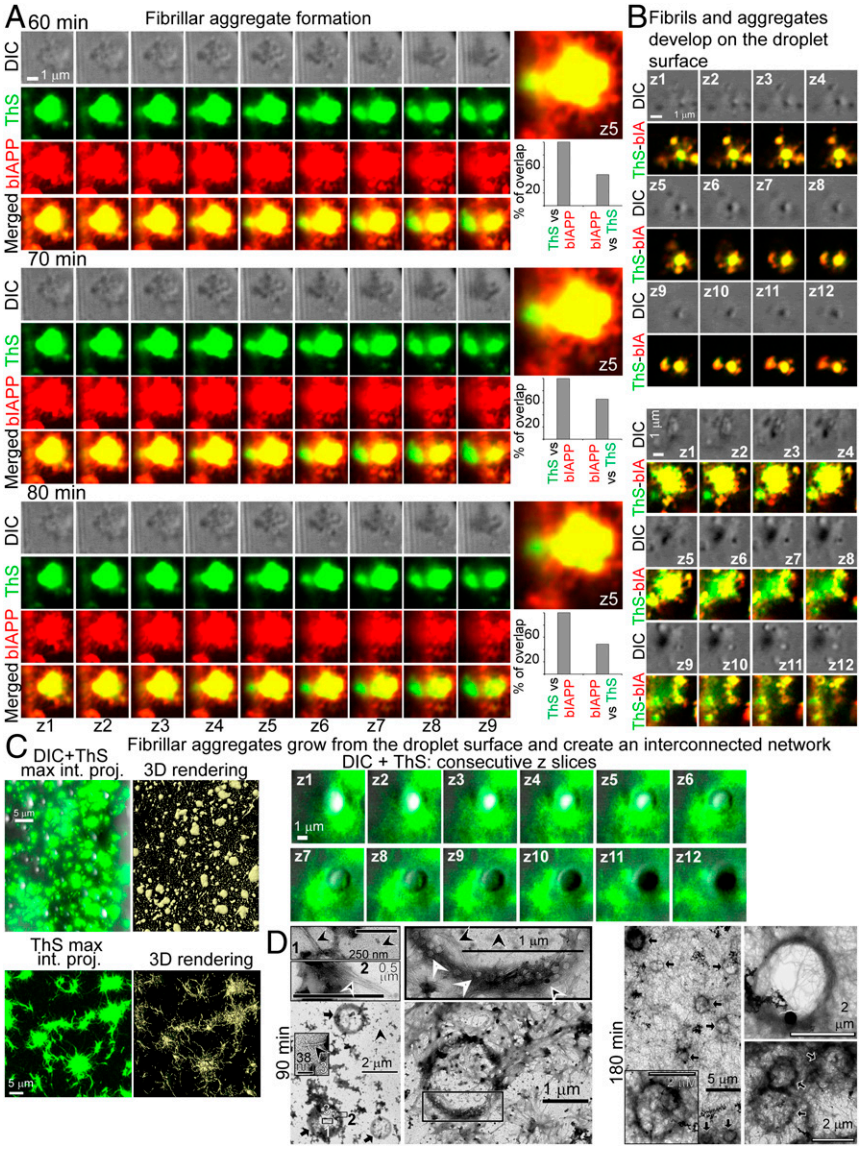

Fig. 4. Fibrils and aggregates grow from the droplet surface and create an interconnected fibrillar network. (*A*) Aggregation. Consecutive z slices from reactions at 60, 70, and 80 min (*Left*). z5 zoom up: aggregate being the most in focus (*Top Right*). All images have identical display settings, identical to Fig. 3*B* for comparison. Overlap percentage between the two fluorophores within z5 (*Bottom Right*). (*B*) Fibrils (*Top*) and fibrillar aggregates (*Bottom*) develop on the droplet surface. Consecutive z slices from a 60-min reaction. All images have identical display settings. (*C*) At 150 min, hIAPP form fibrillar aggregates, growing from the droplet surface and interconnecting with one another. Maximum intensity projection (max. int. proj.), with a rendered surface of fibrillar aggregates (*Left*, Airyscan mode). ThS labels fibrillar aggregates on the droplet surface and the droplet interior, indicating amyloid cross-β nature (z slices, *Right*). (*D*) TEM of negatively stained hIAPP LLPS reactions at 90 and 180 min confirming the fibrillar nature of the species observed by confocal microscope. Arrowheads: black, fibril within droplets; black-white, fibrils growing from the droplet surface; white, fibrils extending from within the droplet to outside. *Insets*: zoom up. Arrow: droplet.

Insulin Modulates hIAPP. Within secretory granules, hIAPP is present in millimolar without aggregating, despite fibrillizing in vitro at low micromolar. Insulin is costored with hIAPP in granules and can inhibit hIAPP fibrillization in vitro (16). In vivo, changes in hIAPP:insulin ratios are observed and differences in ratio have long been postulated to explain hIAPP aggregation and possibly pathology (17–19). Therefore, we assessed the effects of four different insulin:hIAPP ratios on hIAPP LLPS, hydrogelation, and aggregation. Insulin alone did not undergo LLPS (*SI Appendix*, Fig. S2*A*). For every insulin concentration tested, hIAPP underwent LLPS at the AWI before propagating into the bulk, and droplets contained hIAPP (bIAPP labeling) (Fig. 6 *A* and *B*, Movie S5, and *SI Appendix*, Fig. S2*A*). However, insulin delayed the onset of hIAPP LLPS: 22.6-fold with 141.9 μM insulin (1:1), 6.3-fold with 42.3 μM insulin (1:3.4), 3.2-fold with 12.9 μM insulin (1:11), and 3-fold with 2.94 μM insulin (1:50) (Fig. 6 *B* and *J*). The effect became concentration independent below 1 insulin:11 hIAPP. Moreover, as insulin concentration increased, fewer droplets formed overall, particularly in the bulk. For a while post-LLPS, mostly bIAPP-avidin-TR fluorescence was detected and, in contrast to hIAPP alone, very little ThS labeling was (Fig. 6 *A*–*C* and *SI Appendix*, Fig. S2*A*). The droplets possessed liquid-like property as they underwent fusion and hIAPP molecules freely diffused within droplets (Fig. 6 *D* and *E* and *SI Appendix*, Fig. S2*B*). Hydrogelation within droplets (~70 to 80% immobility) was delayed, ~1.6-fold by 12.9 μM insulin and ~1.4-fold by 42.3 μM insulin (Fig. 6 *E* and *J* and *SI Appendix*, Fig. S2*C*). However, delay of the early phases of droplet hydrogelation showed insulin concentration dependence. Indeed, molecular mobility within droplets at ~50 min was enhanced ~1.2- and 1.6-fold with 12.9 and 42.3 μM insulin, respectively. Insulin also delayed droplet impermeable coat formation (measured by molecular exchange between droplet and bulk) by 51-fold for 12.9 μM and 46-fold for 42.3 μM (Fig. 6 *F* and *J* and *SI Appendix*, Fig. S2*D*). Moreover, insulin delayed hIAPP aggregation from droplet surfaces and aggregation interconnecting droplets together by ~6-fold, and aggregate meshwork formation by ~19-fold (Fig. 6 *G*, *H*, and *J* and *SI Appendix*, Fig. S2*E*). Insulin also delayed ThS labeling, with bIAPP labeling overlap with that of ThS increasing progressively (from <10 to 85%) and becoming high only after aggregation had occurred (Fig. 6*I*). Altogether, these experiments demonstrate that insulin is not an inhibitor but a modulator of hIAPP, as insulin only delays hIAPP LLPS, droplet hydrogelation, droplet impermeable coat formation, and aggregation.

At the AWI, the Whole hIAPP System Transitions Between a Soluble and Hydrogel State. We then investigated what happens to small aggregates derived from droplet maturation (beyond initial LLPS). We used 4 μM hIAPP (for direct comparison with our previous studies), and designed an experimental setup (*SI Appendix*, Fig. S3). In H_2O, highly mobile hIAPP-bIAPP avidin fluorescein aggregates accumulated over time at the AWI, before becoming immobile (Fig. 7*A* and Movie S6). We previously demonstrated rheologically that 4 μM hIAPP undergoes hydrogelation (6). Therefore, we interpreted the increased aggregate immobility as evidence of their entrapment within a forming hydrogel in the whole system. At 18 h, the system was heterogeneous as aggregate number and distribution between replicates was different. We previously showed that D_2O abolished variation of the kinetics of hIAPP fibrillization and hydrogelation. D_2O reduces H bond formation between solvent and proteins, due to a reduced exchange frequency of solvent molecules, leading to a decrease in protein hydration (20). To reduce the surface area in contact with D_2O, proteins adopt more compact structures or associate into aggregates by increasing hydrophobic intermolecular interactions (20, 21). Therefore, a difference between a reaction rate in D_2O versus that in H_2O can provide clues as to the reaction mechanism in term of hydration versus intramolecular interactions. In D_2O, the AWI-accumulated aggregates, became immobile more rapidly and more were detected (Fig. 7*B* and Movie S7). The system at 18 h was more homogeneous than in H_2O, with aggregate number and distribution similar between replicates.

bIAPP is a direct assembly reporter due to its incorporation, but it affects the process (Fig. 1). Therefore, we used other nonincorporating reporters, one of which is a newly characterized BODIPY-derived molecular rotor. Molecular rotors belong to a subset of twisted intramolecular charge transfer (TICT) excited state fluorophores, with a viscosity-dependent fluorescent emission (22). TICT rotation (low viscosity) favors the population of lower energy charge transfer states with decreased emission intensity and quantum yield (i.e., no fluorescence emission). Interference with TICT rotation (viscosity increase) favors the radiative pathway and results in a decrease in TICT nonphotonic relaxation and a larger quantum yield of fluorescent relaxation (i.e., fluorescence emission) (23). BODIPY rotors have strong UV absorbance, are stable in physiological conditions, but are normally delocalized or nonspecifically localized (24). A BODIPY conjugated via a linker to benzylguanine (BG-BODIPY) was developed to report local viscosity changes (relevant to our study) and for targeting to specific cellular locations (relevant to cellular studies) (25).

BG-BODIPY (green fluorescence) and 0.2 μm green fluorescent beads detected aggregates accumulating at the AWI, becoming immobile, with D_2O promoting every aspect, similarly to bIAPP (Fig. 7 *C*–*F* and Movies S8–S11). However, the clusters were bigger. The AWI gelled aggregates trapped neighboring bulk assemblies to form larger gelled clusters spreading into the bulk, suggesting that hydrogelation also spread into the bulk (Fig. 7*G* and Movie S12). Controls (fluorophores alone) showed that aggregation and immobility were solely due to hIAPP (*SI Appendix*, Fig. S4). These results show that the whole hIAPP system transitions between a soluble and hydrogel state, starting at the AWI and propagating into the bulk.

To ascertain that BG-BODIPY and beads reported hIAPP assembly, we used double labeling. BG-BODIPY and bead clusters (green) overlapped those of bIAPP-avidin-TR (red) (Fig. 7 *H* and *I*). Double-labeled pixel quantification yielded an overlap coefficient of 0.748 for BG-BODIPY-bIAPP, with 97.4% of BG-BODIPY colocalizing with bIAPP, and 49.5% of bIAPP colocalizing with BG-BODIPY. Although the overlap coefficient was high (0.821) for beads-bIAPP, double-labeled structures often had adjacent single-labeled features. Indeed, 33.7% of beads colocalized with bIAPP, and 23.8% of bIAPP colocalized with beads. This suggests that bIAPP and beads may report different gelled network areas perhaps with different mesh size.

Hydrogelation Timing and Kinetic Variation within the Whole System. From aggregate tracking at the AWI, we determined their trajectories, and quantified the speed and duration of aggregate mobility. For every reporter, movement occurred mostly early (green versus red) and aggregates moved less, over shorter distances and for shorter time periods in D_2O (Fig. 8 and *SI Appendix*, Fig. S5). bIAPP and 0.2 μm beads reported similar gelation times (4.29 ± 1.05 and 5.21 ± 1.07 h, respectively, in H_2O; and 2.99 ± 0.08 and 2.81 ± 0.37 h, respectively, in D_2O), within a similar range but slower than our previous rheology (~2 [fast regime] to 6 h [slow regime] in H_2O, and uniformly ~2 h in D_2O) (Fig. 8 *A* and *C*) (6). This suggests that beads might inhibit assembly as did bIAPP. At early time points, gaps in the tracking are due to the high spatial density of very small beads and their fast movement. In contrast, BG-BODIPY reported quicker gelation times, 1.26 ± 0.72 h in H_2O and 0.65 ± 0.23 h in D_2O (Fig. 8*B*). Graphs of SD over mean show that the system was more heterogeneous in H_2O and that variation was maximal before gelation started.

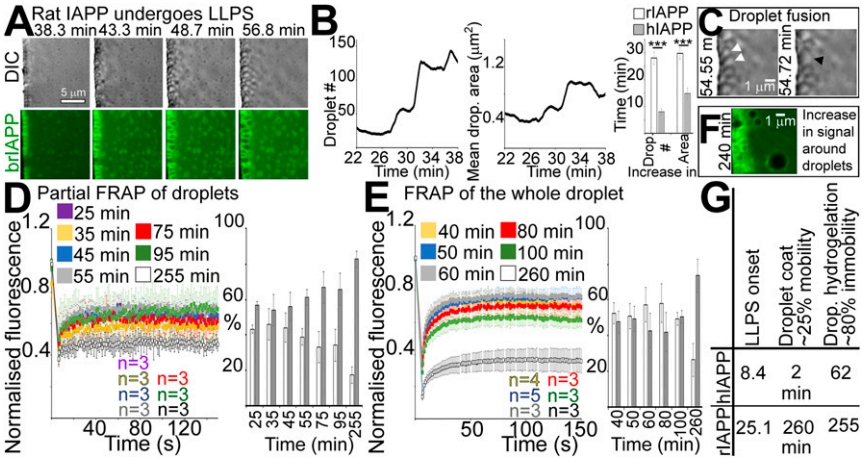

Fig. 5. rIAPP undergoes LLPS, with the droplets in a liquid-like state and not aggregating. (*A*) rIAPP droplet accumulation and size increase over time (Movie S4). (*B*) Timing of droplet appearance and size increase (plots: representative of three independent replicate; bar graph: $n = 3$, $^{***}P < 0.0004$). (*C*) rIAPP droplets fuse (white arrowheads) and relax into larger droplets (black arrowhead). (*D*) Droplet internal rearrangement of rIAPP molecules at different times after LLPS onset. brIAPP fluorescence intensity recovery within a droplet bleached region, and fraction of mobile/immobile molecules. n = droplet number analyzed from at least three independent replicates. (*E*) rIAPP molecule exchange between droplets and bulk at different times after LLPS onset. brIAPP fluorescence intensity recovery within whole bleached droplets, and fraction of mobile/immobile molecules. n = droplet number analyzed from at least three independent replicates. (*F*) brIAPP labeling increased over time at the AWI, within and around droplets, but without aggregate formation. (*G*) Summary of the timings for LLPS and associated processes for hIAPP and rIAPP. Drop.: droplet.

At the AWI, Interconnected Aggregates Form Clusters, which Grow and Fuse Together. We then investigated whether aggregates within a cluster were connected to each other and moving coordinately. For BG-BODIPY in D_2O (which resulted in the biggest and most numerous clusters), aggregates moved together in local flow fields to form interconnected clusters, as early as <0.47 h (Fig. 9*A*). Individual connected aggregate clusters grew over time, rapidly fused together (<1 min Fig. 9*B*, <3 min Fig. 9*C*) to form bigger clusters that carried on evolving and growing (Fig. 9 *B* and *C*). Aggregate connectedness and cluster fusion were also seen with BG-BODIPY in H_2O, although not as clearly, at later stages and over longer time periods (~82 min) (*SI Appendix*, Fig. S6). For bIAPP and 0.2 μm beads, only assays in D_2O showed clear cluster fusion, slow with bIAPP and rapid with beads (*SI Appendix*, Figs. S7 and S8). This is not surprising as D_2O promotes amyloidogenesis, and bIAPP and beads delay it. Our experiments demonstrate that aggregates, first originating from LLPS droplet maturation, further grew and matured at the AWI to create a macroscopic network of interconnected aggregate clusters. This network further evolved into a gelled meshwork, which propagated into the bulk.

The Microviscosity of the AWI-Adsorbed hIAPP Layer Increases over Time, with D_2O Promoting Higher and More Homogeneous Microviscosity. Fluorescence lifetime imaging (FLIM) allows efficient measurement and mapping of microviscosity via the concentration-independent, but viscosity-dependent, lifetime decay of the molecular rotor (26). We first ascertained that BG-BODIPY fluorescence lifetime in a nonviscous solution was not decaying (*SI Appendix*, Fig. S9*A*) and that its fluorescence lifetime linearly increased with increased viscosity (Fig. 10*A*). Then, we incubated hIAPP reactions with BG-BODIPY for either 5 (gelled but not fully mature AWI-adsorbed layer) or 21 h (gelled AWI-adsorbed layer at equilibrium), in H_2O or D_2O. For all reactions, the measured BG-BODIPY lifetime decay curves gave good fits ($\chi^2 \sim 1$) (*SI Appendix*, Fig. S9*C*). For the 5-h reactions, we observed a range of fluorescence lifetime distribution with the mean main peak for all replicates at ~364 ps in H_2O and 383 ps in D_2O, corresponding to viscosities of 14.3 and 15.7 cP, respectively (Fig. 10 *B* and *C* and *SI Appendix*, Fig. S9*B*). For the 21-h reactions, the mean main peaks of fluorescence lifetime for all replicates were at ~1,498 ps in H_2O and 2,082 ps in D_2O, corresponding to viscosities of 184.9 and 335.7 cP, respectively. Therefore, the microviscosity of the AWI-adsorbed gelled layer increased as the layer matured. The viscosity was not uniform across the AWI (regions of higher viscosity) and the lifetime and viscosity range became narrower and homogeneous in D_2O. For each condition, the bulk, up to the well edge in some cases, was also viscous.

Discussion

Our study was motivated by a desire to understand the triggers of initial amyloid aggregation and how the system further evolves into a pathological aggregated state. LLPS is involved in the physiological formation and maintenance of membraneless organelles, but also linked to pathology due to irreversible hydrogelation through amyloid-like aggregation (10, 12, 13). In most cases, the proteins involved contain low-complexity domains (LCDs) driving LLPS (e.g., FUS and hnRNPA1) (11, 12). To date, only our study on hIAPP and another very recent on human tau showed that polypeptides not containing defined LCDs can also undergo LLPS (15).

In the first part of our study, we demonstrated that hIAPP underwent LLPS by forming spherical liquid droplets, which fused and relaxed into bigger droplets, and contained freely diffusing hIAPP molecules. LLPS first occurred at the AWI before propagating into the bulk. Similarly, a high concentration of ptau441 by itself only underwent LLPS from the AWI, indicating LLPS dependence on an increase in critical local protein concentration (15). In contrast to most studies, we did not change the experimental conditions to increase local concentration, e.g., crowding agent addition. We show that AWI absorption increased sufficiently the local concentration of amphiphilic amyloid precursors in localized "pockets" to trigger LLPS. Previously, we demonstrated that AWI adsorption is critical for both amyloid precursor nucleation and fibrillar species (4, 7). We can now extend further the AWI role to steps preceding nucleation, namely LLPS. At low hIAPP concentrations, droplets, the AWI and aggregates all became ThS-positive concomitantly. We envisage AWI adsorption of precursors driving two simultaneous competing processes: fast LLPS and LLPS-independent nucleated aggregation. LLPS would require a higher localized precursor concentration, whereas aggregation

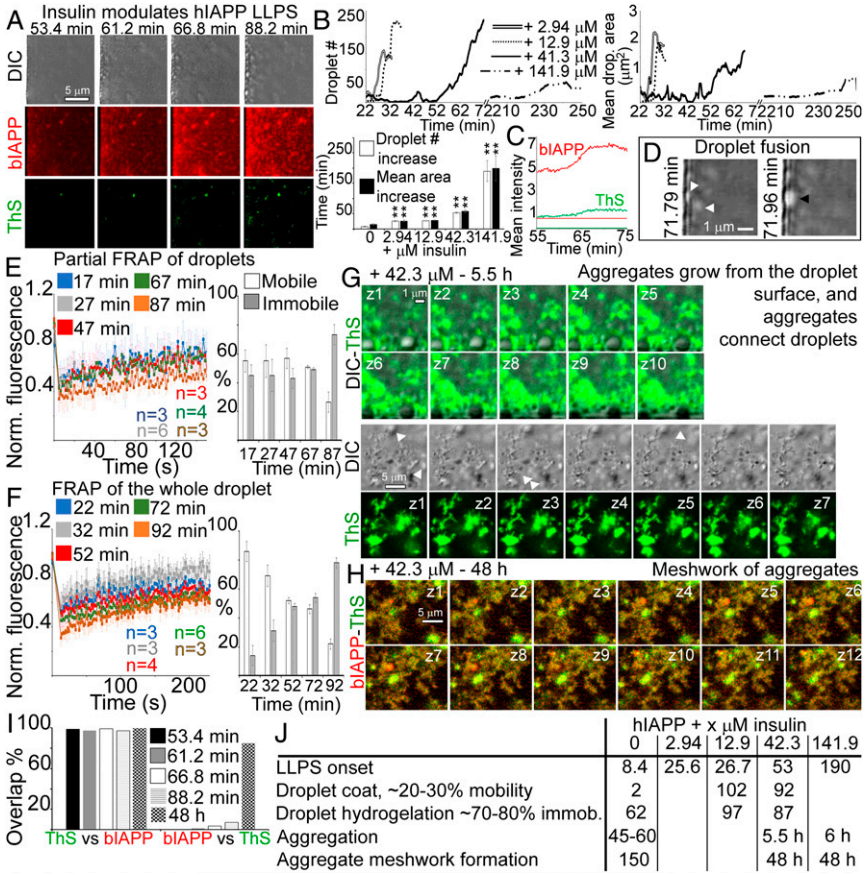

Fig. 6. Insulin modulates hIAPP. (*A*) Insulin delays hIAPP LLPS (Movie S5). A total of 129 µM hIAPP-12.89 µM bIAPP-1.28 µM avidin-TR-100 µM ThS was incubated with 42.3 µM insulin. (*B*) Insulin effect is concentration dependent but not linear. Quantification of the timing of droplet appearance and size increase (plots: representative of three independent replicates; bar graph: $n = 3$, $^{**}P < 0.02$ when compared to hIAPP alone). (*C*) Mean intensity of ThS or bIAPP-avidin-TR within droplet interiors of a hIAPP-42.3 µM insulin reaction. Background fluorescence (horizontal lines) was measured from bulk fluorescence at t0. (*D*) hIAPP-42.3 µM insulin droplets fuse (white arrowheads) and relax into larger droplets (black arrowhead). (*E*) Droplets internal rearrangement of hIAPP molecules in presence of 42.3 µM insulin at different times after LLPS onset. bIAPP-avidin-TR fluorescence intensity recovery within a droplet bleached region, and fraction of mobile/immobile molecules. n = droplet number analyzed from at least three independent replicates. Norm.: normalized. (*F*) hIAPP molecular exchange between droplets and bulk in presence of 42.3 µM insulin, at different times after LLPS onset. bIAPP-avidin-TR fluorescence intensity recovery within whole bleached droplets, and fraction of mobile/immobile molecules. n = droplet number analyzed from at least three independent replicates. Norm.: normalized. (*G*) 42.3 µM insulin delays hIAPP aggregation on the droplet surface (*Top*) and droplet interconnection by aggregates (*Bottom*). Consecutive z slices (Airyscan mode). (*H*) 42.3 µM insulin delays formation of interconnected aggregate meshworks. Consecutive z slices (Airyscan mode). (*I*) Overlap percentage between ThS and avidin-TR labeling over time for hIAPP-42.3 µM insulin. (*J*) Summary of the timings (in minutes unless otherwise stated) for LLPS and associated processes for hIAPP alone and in presence of insulin. Immob: immobility.

would require fewer precursors for nucleation. At high hIAPP concentration (129 and 32 µM), LLPS initially dominates due to a high precursor concentration into localized AWI pockets and because it is faster than aggregate nucleation. This would deplete precursors from the surrounding solution and delay LLPS-independent aggregation. At intermediate concentration, AWI adsorption of precursors would decrease, LLPS onset would be delayed, and aggregation increased (e.g., 16 and 8 µM). At low concentration, LLPS would be further delayed, allowing aggregation to dominate (4 µM). Over time at high hIAPP concentration, the precursors became even more spatially restricted and concentrated within droplets, which triggered hydrogelation. In contrast to FUS reversible hydrogelation, our FRAP and TEM data suggest that hIAPP droplet hydrogelation became very rapidly irreversible and this was due to fibrillization within droplets (27). Quickly after LLPS onset, droplets acquired an impermeable coat, preventing molecular exchange with the solution. The loss of molecular diffusion within droplets was more progressive and slower. Therefore, droplet hydrogelation required very limited molecule recruitment from the bulk. Similar droplet properties were observed for tau (15). hIAPP and tau differ from FUS as they do not possess a LCD. FUS LCD has been implicated in LLPS and hydrogelation and might be responsible for its gel reversibility (11, 27). Our results also suggest that hIAPP LLPS was arrested by hydrogelation. Following hydrogelation, we observed fibrillization from the droplet surface, which further evolved into an aggregate network interconnected by fibrils. As droplets mature, their surface also changes (e.g., surface tension). Internal hIAPP would be coming out of solution at the droplet surface, which would be supersaturated in aggregation-prone and fibrillizing species, as confirmed by TEM. Droplet hydrogelation, fibril protrusion from droplets, and droplet maturation into aggregates, were described for other amyloids (12, 15). Moreover, LLPS of tau microtubule-binding repeats was concomitant with an increase in β-sheet structures promoting fibrillization in the presence of heparin (28).

Using two reporters, we showed that separate discrete areas within the whole reaction and at the droplet level can be detected. bIAPP should incorporate in any assembly stages. However, ThS fluorescence detection (450-nm excitation, 488-nm emission), combined with its detection threshold, should indicate stacked β-sheet assemblies (i.e., beyond nuclei). We cannot rule out that some ThS fluorescence arose from rotation hindrance due to the

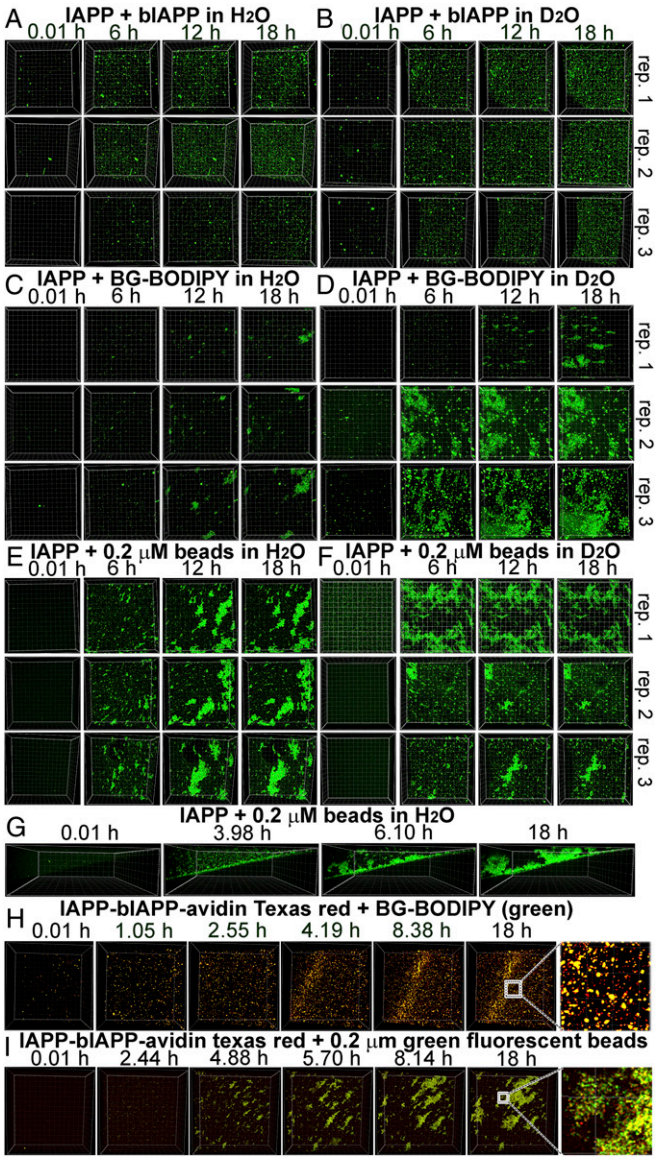

Fig. 7. In the whole system, hIAPP aggregation at the AWI forms clusters. (*A–F*) hIAPP aggregates accumulate at the AWI, forming "clusters" that become immobile. The 3.6 μM hIAPP-0.4 μM bIAPP-0.08 μM avidin D fluorescein in H_2O (*A*) or D_2O (*B*), 4 μM hIAPP-5.56 μM BG-BODIPY (green) in H_2O (*C*) or D_2O (*D*), 4 μM hIAPP-9.5 ± 0.4 × 10^5 0.2 μm green fluorescent beads in H_2O (*E*) or D_2O (*F*). Three-dimensional projections of z stacks (AWI facing the experimentalist and bulk behind) at relevant time points ($n = 3$ for each condition) (Movies S6–S11). (*G*) hIAPP aggregation spreads into the bulk (Movie S12). Four μM hIAPP-0.2 μm beads in H_2O. Three-dimensional projections with the AWI viewed from the side and bulk above. BG-BODIPY (*H*) or 0.2 μm beads (*I*) colocalize with hIAPP. The 3.6 μM hIAPP-0.4 μM bIAPP-0.08 μM avidin D-TR in H_2O was incubated with 5.56 μM BG-BODIPY (green) or 0.2 μm green fluorescent beads. Three-dimensional projections of z stacks (AWI facing the experimentalist and bulk behind) at relevant time points. *Right*: dashed box zoom up.

droplet interior crowded environment. However, this effect would be homogeneous within droplets, and less prominent outside droplets. We clearly observed discrete, nonhomogeneous, and weak ThS labeling within droplets where viscosity should be at its highest (Fig. 3*B*) and a strong ThS positivity outside droplets and in fibrillar projections (Fig. 4 *B* and *C*). Thus, we believe that ThS predominantly reported an increase in β-sheets, and that the hIAPP species triggering droplet formation were not in a stacked β-sheet conformation (sparse and weak ThS labeling). TEM confirmed the amyloid fibrillar nature of the ThS-positive species. The AWI first acquired stacked β-sheet species (ThS positivity) before they spread into the bulk. For droplets, their surface acquired hIAPP species that converted over time into stacked β-sheets (within 20 to 30 min), leading to strong ThS labeling and to fibrils encircling the surface (TEM). This is consistent with rapid formation of an impermeable coat around droplets, as seen by FRAP. Within droplets, labeling by both reporters increased over time (up to 45 min), before decreasing (when surface aggregate became apparent). This suggests that droplet surface saturation, and initial aggregation, might occur by recruitment of a significant proportion of species from within droplets. This is consistent with hIAPP molecules within droplets freely diffusing up to 52 min. The main fraction of recruited species was more likely to be nonstacked β-sheet, as ThS labeling only decreased slightly before plateauing, whereas bIAPP labeling significantly plateaued before decreasing progressively. These observations, combined with TEM, suggest that gelled droplet cores are maintained by ThS-positive stacked β-sheet species (fibrils within droplets by TEM), and the ThS-negative nonstacked β-sheet species are attracted to droplet surfaces to promote aggregation (no fibril layer encircling the droplet surface by TEM at 90 min) (*SI Appendix*, Fig. S10).

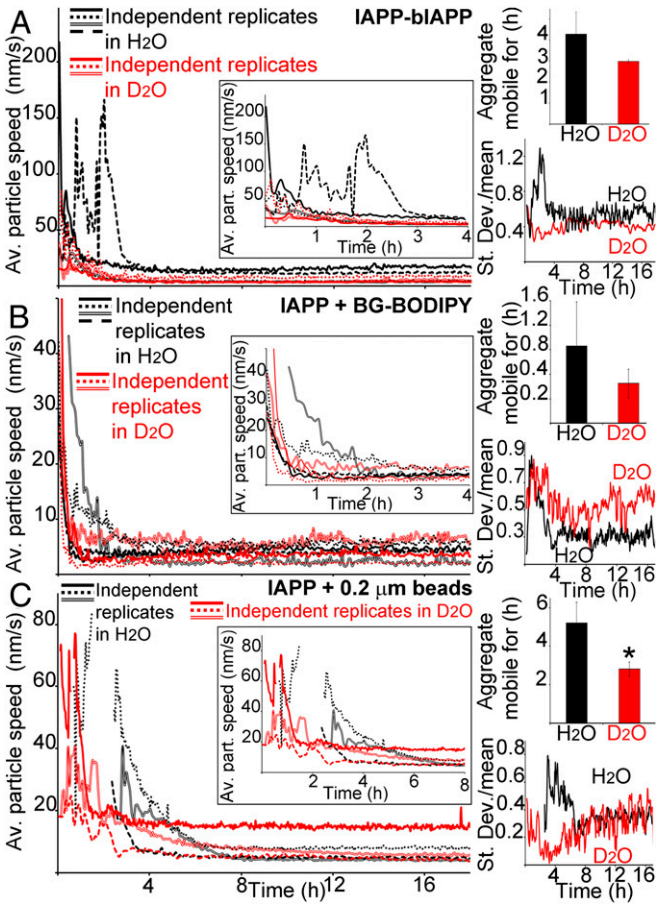

Fig. 8. At the AWI, hIAPP aggregates move less and stop moving more quickly in D_2O than in H_2O, with the system being more homogeneous in D_2O. AWI aggregates of Fig. 7 were tracked, and aggregate speed was calculated, along with that of mean flow. Average (Av.) particles (part.) speed with that of mean flow subtracted over time for 3.6 μM hIAPP-0.4 μM bIAPP (*A*), 4 μM hIAPP-5.56 μM BG-BODIPY (*B*), 4 μM hIAPP-9.5 ± 0.4 × 10^5 0.2 μm beads (*C*), in H_2O or D_2O. *Insets*: early time point zoom up. Aggregate mobility duration was calculated from the *Left* panels (*Top Right*). Variation coefficient (SD over mean) over time (*Bottom Right*). Error bars ± SEM *$P < 0.05$.

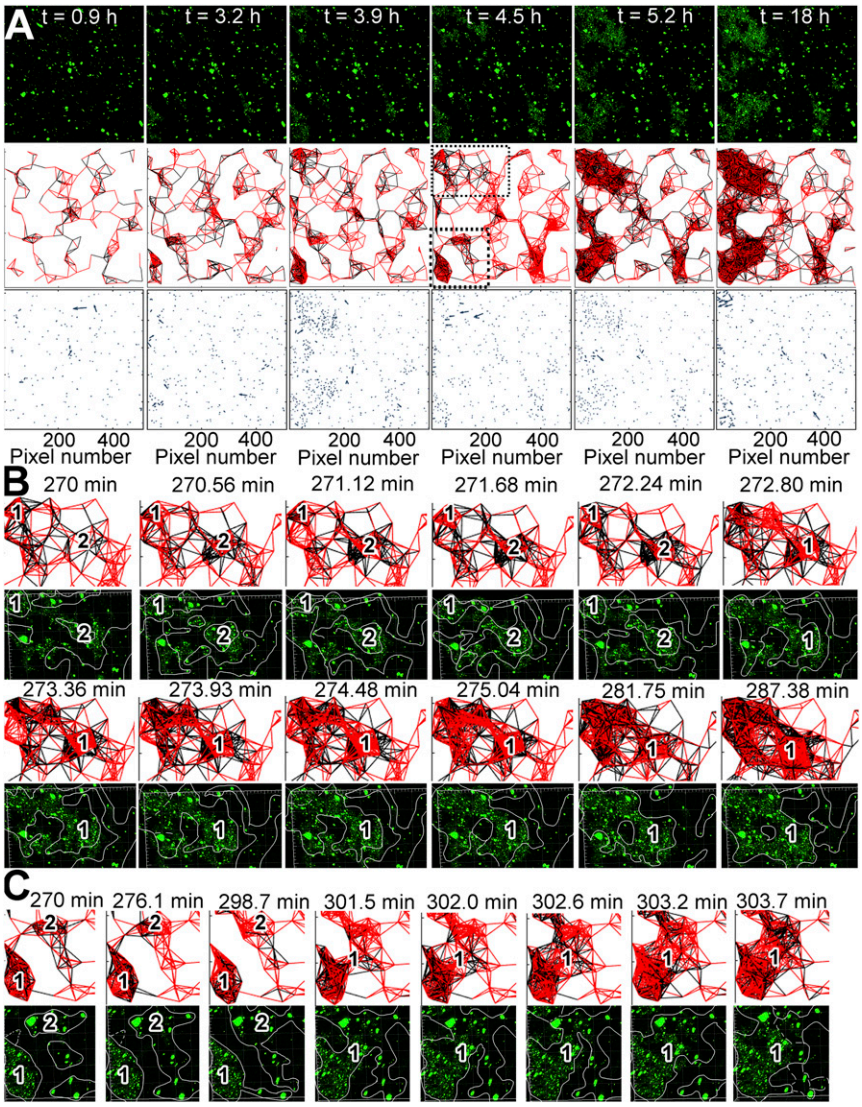

Fig. 9. At the AWI, connected hIAPP aggregates move coordinately in local flow fields, form individual clusters that grow and fuse together. Four μM hIAPP-5.56 μM BG-BODIPY (green) in D_2O. From aggregate tracking (Fig. 8), movement vectors and aggregate connectivity were determined. (*A*) Maximum intensity projections of an 18-h time course (*Top*), aggregate connectivity (red line: aggregates moving in the same direction, connectedness; black line: aggregates moving in opposite direction, nonconnectedness) (*Middle*), and movement vectors (*Bottom*). Dashed boxes: areas further examined in *B* and *C*. (*B* and *C*) Examples of aggregate connectivity (*Top*) and corresponding 3D projections (*Bottom*). Numbers indicate individual clusters of connected aggregates that evolve over time. White lines: connected aggregate clusters (projection and connectedness were superimposed and lines drawn around connected aggregates).

Using rIAPP, we show that LLPS does not rely on hIAPP amyloidogenic sequence, whereas droplet hydrogelation, impermeable coat formation in a physiological time frame, and aggregation do. However, the amyloidogenic sequence does accelerate LLPS. Thus, due to its nonamyloidogenicity and nontoxicity, rIAPP may represent normal physiology. This suggests that IAPP LLPS is a normal physiological process, and that droplet hydrogelation and coat formation have to be delayed sufficiently to prevent aggregation in a time frame relevant for granule formation and secretion. Various amyloids initially undergo LLPS without aggregating (15). Therefore, amyloid LLPS might have functional roles, e.g., maintaining a local pool of rapidly available molecules. However, LLPS also requires tight control as it increases the local concentration of aggregation prone polypeptides, which could convert into pathological aggregates.

IAPP and insulin are coexpressed in β-cells, costored in and cosecreted from their secretory granules. We demonstrate that insulin only delayed hIAPP LLPS, droplet hydrogelation, impermeable coat formation, and aggregation. Monomeric insulin binds to soluble hIAPP and preformed fibrils, and prevents β-sheet conversion, which may explain how insulin delays hIAPP LLPS (29). Thus, insulin may modulate hIAPP amyloidogenic processes to prevent pathology on a physiological time frame, i.e., delaying aggregation to allow normal secretion (~10% of granules are turned over every hour during active secretion) (30). In healthy pancreatic cells, hIAPP might undergo LLPS to increase local concentration of granule components to trigger packaging in granules and granule formation. The insulin effects were nonlinear, underlining the importance of hIAPP:insulin ratio. Although IAPP:insulin molar ratio in whole granules is 1 to 2:50, IAPP is found in the halo, crystalline hexameric insulin in the core, and insulin concentration in the halo is unknown (2). Moreover, the oligomerization interface of insulin B-chain monomers and dimers, which is buried in hexamers, binds preferentially to hIAPP monomer amyloidogenic region, suggesting that only "soluble" insulin found in the halo could bind hIAPP (31). Insulin–IAPP coexpression/secretion can be altered in favor of IAPP (e.g., increased IAPP expression or secretion, or reduced insulin secretion) (17–19). Intercellular heterogeneity of IAPP content, but not of insulin, also exists among β-cells with interislet variations in β-cell functions (32). Therefore, insulin–hIAPP ratio differences between and within cells, along with alteration of their parallel expression, may locally shift LLPS toward pathological aggregation. This is consistent with mild hIAPP amyloid deposition in islets of nondiabetic individuals, and with transient IAPP overproduction in cats without diabetes but with impaired glucose tolerance (33, 34). In TIID, IAPP deposition affects β-cell functionality, cell-to-cell contacts, and

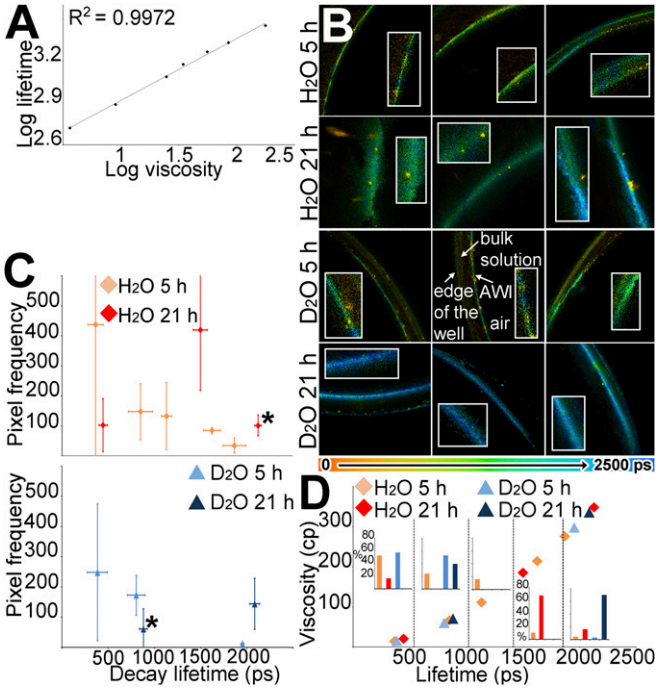

Fig. 10. The viscosity of the AWI-adsorbed hIAPP layer increases over time, with D_2O promoting higher and more homogeneous viscosities. (*A*) BG-BODIPY is viscosity sensitive. FLIM performed on BG-BODIPY-glycerol solutions of increased viscosities (28 to 630 cp), and fluorescence decay lifetime was determined. Linear relationship between the log of BG-BODIPY decay lifetime and the log of glycerol viscosity, with a very good fit. (*B*) FLIM images of the AWI region of 4 μM hIAPP-5.56 μM BG-BODIPY reactions, in H_2O or D_2O, at 5 or 21 h ($n = 3$ per condition). *Insets*: zoom up of representative AWI regions containing several fluorescence lifetime values (with brightness being increased). Lookup table: colors assigned for each fluorescence lifetime value, from red (short lifetime) to blue (long lifetime). (*C*) Fluorescence lifetime distribution. For each condition, fluorescence lifetimes and pixel frequencies for each peak were assigned from the histograms of fluorescence lifetime distribution (*SI Appendix*, Fig. S9). $n = 3+$ with multiple fields of view analyzed per replicate. Error bars ± SEM. *: lifetime peaks seen in fewer than three analyzed images. (*D*) Viscosity corresponding to fluorescence lifetime was assigned using the calibration curve from *A*. Dotted lines: lifetime segregation into five groups. Bar graphs: lifetime proportion for each condition within each group.

overall islet architecture (35, 36). In turn, insulin production/secretion would be reduced drastically, causing TIID systemic effects but also contributing to pathogenesis by failing to prevent hIAPP aggregation. Moreover, IAPP intracellular deposition (cytoplasm, and in granule halo near membranes) could lead to β-cell death (apoptosis due to ER stress, ubiquitin–proteasome dysregulation, lysosomal damage, or lysosomal extrusion after crinophagy of unused granules) (2, 37). Released extracellular fibrillar species could seed aggregation of secreted hIAPP from nonaffected cells, leading to further cell death.

In the second part of our study, we show that LLPS-derived hIAPP aggregates grew to form macroscopic clusters, inside which aggregate connectedness and coordinate movement were observed. Over time these clusters grew, fused, and evolved via internal rearrangement, eventually percolating the whole system, spreading from the AWI into the bulk. Hydrogelation kinetics of the whole system in H_2O were complex. With BG-BODIPY in H_2O, the only reporter not delaying assembly, aggregates stopped moving ∼1.3 h with huge variation, consistently with our previous rheological work (gelation onset ∼0.5 to 2 h with full gelation within 3 to 22 h) (6). In D_2O, cluster fusion was also quicker (<0.47 h, 0.3 h by rheology), and the AWI gelled layer microviscosity was higher. D_2O weakens molecule solvation and increases aggregation, which should accelerate cluster formation and hydrogelation (38). Our results suggest that hydrogen bonding between hIAPP aggregates is more important than that with solvent. The hydrogelation kinetic variations in H_2O could be explained by LLPS, during which the system evolves independently from multiple pathways generated from varying droplet number. Due to the system finite size and after a transient period, only a few phase-separated droplets should coexist with gelation occurring within each. Droplets mature into aggregates, which form clusters that grow and eventually the whole system percolates. As clusters grow more rapidly in D_2O, the coexistence of multiple clusters is eliminated with the system behaving as a "one-cluster," leading to a decrease in stochastic variations (i.e., homogeneous kinetics). Hydrogelation heterogeneity in H_2O could represent stochastic variations between one-cluster versus "two-cluster" systems, during the transient period. In D_2O, the replicate average speed traces were almost identical and the overall system variation extremely low, demonstrating that gelation occurred concomitantly in all replicates (i.e., a predominant one-cluster system formed very rapidly).

We propose that hIAPP phase-separated liquid droplets undergo hydrogelation before maturing into aggregates, processes depending on the amyloidogenic sequence and modulated by insulin (*SI Appendix*, Fig. S10). Aggregation at the droplet surface leads to the formation of a fibrillar network connecting droplets and aggregates together, which further grows to form macroscopic clusters, supporting further aggregation. Macromolecular interactions between aggregates within clusters are initially transient, allowing coordinate aggregate movement and internal rearrangement. The clusters provide a microenvironment spatially organizing aggregates and increasing their local concentration, which promotes formation of more definite long-range macromolecular interactions (e.g., fibril entanglement). This triggers the whole system hydrogelation, initially as a "loose" immature hydrogel, until optimal volume shrinking and network strength are achieved, i.e., hydrogelation equilibrium and the fibrillar meshwork is at its tightest. The microviscosity increase observed during maturation of the AWI-adsorbed gelled layer corroborates this.

To conclude, our key results are that pathological hIAPP amyloidogenesis occurs via hydrogelation of phase-separated droplet and aggregation. The existence of different states for the same amyloidogenic polypeptide may allow different toxic mechanisms. The phase-separated state would concentrate toxic species early in the process, but also impact on membrane by changing their curvature (surface tension effects) (39). Furthermore, nonnatural amyloid hydrogelation could physically change the intracellular and extracellular environments, affecting/disrupting many processes, e.g., permanently trapping cargo and altering extracellular matrix properties (10, 40, 41). Altogether, the consequences of these effects could be critical for membrane integrity and overall cellular functions, in particular at sites where physiological hydrogels are absent or have different properties. Finally, understanding LLPS misbalance and malfunction may provide insights into a novel common pathological mechanism behind amyloid diseases.

Materials and Methods

Peptides and Reagents. Peptides and reagents can be found in *SI Appendix, Materials and Methods*.

Fibrillization. Four μM hIAPP, or 3.6 μM IAPP-0.4 μM bIAPP, was incubated with 0.08 μM avidin D-TR (Vector Laboratories Inc) and 32 μM ThT in phosphate-buffered saline (PBS) in a 100-μL reaction volume. Measurement can be found in *SI Appendix, Materials and Methods*.

TEM. TEM procedures can be found in *SI Appendix, Materials and Methods*.

LLPS. A total of 24.81 μL of different IAPP-containing reactions (*SI Appendix, Materials and Methods*) were pipetted on an uncoated glass-bottom dish (MatTek Corporation), and placed within the chamber of a Zeiss LSM 880

Airyscan confocal microscope setup at 25 °C. LLPS was visualized over time using ZEN black (v2.3 SP1), a 63× oil objective, and 0.5% 488- or 561-nm laser power. Analysis is provided in *SI Appendix, Materials and Methods*.

FRAP. IAPP reactions were prepared as in "LLPS." A whole droplet or part of a whole droplet was bleached for 8 s with 30% 405-nm laser power for hIAPP-ThS or brIAPP-avidin fluorescein reactions, or 60% 561-nm laser power for insulin-bIAPP avidin-TR reactions. Recovery was recorded at a 2.1 s/frame rate. Analysis is provided in *SI Appendix, Materials and Methods*.

Aggregate Clustering and Connectedness. hIAPP reactions in PBS in a 345-μL reaction volume, were pipetted in a well of a 96-well plate (black wall, clear bottom). Experimental setup and analysis are provided in *SI Appendix*, Fig. S2 and *Materials and Methods*.

FLIM. A total of 5.56 μM BG-BODIPY was dissolved in solutions containing varying glycerol percentages and fluorescence lifetime was measured. Four μM hIAPP-5.56 μM BG-BODIPY reaction was prepared as in *Aggregate Clustering and Connectedness* and incubated at 25 °C for 5 or 21 h before being placed upside down onto a stage plate holder. Details can be found in *SI Appendix, Materials and Methods*.

Data Availability. All data discussed are available to readers in the paper (main text or *SI Appendix*).

ACKNOWLEDGMENTS. Funding for this work was provided by Synaptica Ltd, Guy Newton translational award, Edward Penley Abraham fund. We thank Drs. Drozdz and Johnson (Pathology, Oxford) for their help with confocal microscopy and TEM respectively, and Niall Moon and Prof. Donohoe for BG-BODIPY synthesis (Chemistry, Oxford).

1. M. Stefani, C. M. Dobson, Protein aggregation and aggregate toxicity: New insights into protein folding, misfolding diseases and biological evolution. *J. Mol. Med. (Berl.)* **81**, 678–699 (2003).
2. P. Westermark, A. Andersson, G. T. Westermark, Islet amyloid polypeptide, islet amyloid, and diabetes mellitus. *Physiol. Rev.* **91**, 795–826 (2011).
3. A. Lomakin, D. B. Teplow, D. A. Kirschner, G. B. Benedek, Kinetic theory of fibrillogenesis of amyloid beta-protein. *Proc. Natl. Acad. Sci. U.S.A.* **94**, 7942–7947 (1997).
4. L. Jean, C. F. Lee, C. Lee, M. Shaw, D. J. Vaux, Competing discrete interfacial effects are critical for amyloidogenesis. *FASEB J.* **24**, 309–317 (2010).
5. E. Y. Chi *et al*., Amyloid-beta fibrillogenesis seeded by interface-induced peptide misfolding and self-assembly. *Biophys. J.* **98**, 2299–2308 (2010).
6. L. Jean, C. F. Lee, P. Hodder, N. Hawkins, D. J. Vaux, Dynamics of the formation of a hydrogel by a pathogenic amyloid peptide: Islet amyloid polypeptide. *Sci. Rep.* **6**, 32124 (2016).
7. L. Jean, C. F. Lee, D. J. Vaux, Enrichment of amyloidogenesis at an air-water interface. *Biophys. J.* **102**, 1154–1162 (2012).
8. R. Kayed *et al*., Permeabilization of lipid bilayers is a common conformation-dependent activity of soluble amyloid oligomers in protein misfolding diseases. *J. Biol. Chem.* **279**, 46363–46366 (2004).
9. M. F. Engel *et al*., Membrane damage by human islet amyloid polypeptide through fibril growth at the membrane. *Proc. Natl. Acad. Sci. U.S.A.* **105**, 6033–6038 (2008).
10. T. Murakami *et al*., ALS/FTD mutation-induced phase transition of FUS liquid droplets and reversible hydrogels into irreversible hydrogels impairs RNP granule function. *Neuron* **88**, 678–690 (2015).
11. A. Molliex *et al*., Phase separation by low complexity domains promotes stress granule assembly and drives pathological fibrillization. *Cell* **163**, 123–133 (2015).
12. A. Patel *et al*., A liquid-to-solid phase transition of the ALS protein FUS accelerated by disease mutation. *Cell* **162**, 1066–1077 (2015).
13. H. J. Kim *et al*., Mutations in prion-like domains in hnRNPA2B1 and hnRNPA1 cause multisystem proteinopathy and ALS. *Nature* **495**, 467–473 (2013).
14. H. LeVine, 3rd, Thioflavine T interaction with synthetic Alzheimer's disease beta-amyloid peptides: Detection of amyloid aggregation in solution. *Protein Sci.* **2**, 404–410 (1993).
15. S. Wegmann *et al*., Tau protein liquid-liquid phase separation can initiate tau aggregation. *EMBO J.* **37**, e98049 (2018).
16. J. L. Larson, A. D. Miranker, The mechanism of insulin action on islet amyloid polypeptide fiber formation. *J. Mol. Biol.* **335**, 221–231 (2004).
17. H. Mulder, B. Ahrén, F. Sundler, Differential expression of islet amyloid polypeptide (amylin) and insulin in experimental diabetes in rodents. *Mol. Cell. Endocrinol.* **114**, 101–109 (1995).
18. T. D. O'Brien, P. Westermark, K. H. Johnson, Islet amyloid polypeptide and insulin secretion from isolated perfused pancreas of fed, fasted, glucose-treated, and dexamethasone-treated rats. *Diabetes* **40**, 1701–1706 (1991).
19. X. Hou *et al*., Prolonged exposure of pancreatic beta cells to raised glucose concentrations results in increased cellular content of islet amyloid polypeptide precursors. *Diabetologia* **42**, 188–194 (1999).
20. A. S. Goryunov, H/D isotope effects on protein hydration and interaction in solution. *Gen. Physiol. Biophys.* **25**, 303–311 (2006).
21. M. J. Parker, C. E. Dempsey, M. Lorch, A. R. Clarke, Acquisition of native beta-strand topology during the rapid collapse phase of protein folding. *Biochemistry* **36**, 13396–13405 (1997).
22. M. K. Kuimova, G. Yahioglu, J. A. Levitt, K. Suhling, Molecular rotor measures viscosity of live cells via fluorescence lifetime imaging. *J. Am. Chem. Soc.* **130**, 6672–6673 (2008).
23. M. A. Haidekker, E. A. Theodorakis, Molecular rotors—fluorescent biosensors for viscosity and flow. *Org. Biomol. Chem.* **5**, 1669–1678 (2007).
24. J. A. Levitt *et al*., Membrane-bound molecular rotors measure viscosity in live cells via fluorescence lifetime imaging. *J. Phys. Chem. C* **113**, 11634–11642 (2009).
25. L. Pytowski *et al*., A novel technique for mapping viscosity in discrete subcellular locations with a BODIPY based fluorescent probe. bioRxiv:10.1101/522532 (19 January 2019).
26. M. K. Kuimova, Mapping viscosity in cells using molecular rotors. *Phys. Chem. Chem. Phys.* **14**, 12671–12686 (2012).
27. Y. Shin *et al*., Spatiotemporal control of intracellular phase transitions using light-activated optoDroplets. *Cell* **168**, 159–171.e14 (2017).
28. S. Ambadipudi, J. Biernat, D. Riedel, E. Mandelkow, M. Zweckstetter, Liquid-liquid phase separation of the microtubule-binding repeats of the Alzheimer-related protein Tau. *Nat. Commun.* **8**, 275 (2017).
29. E. T. Jaikaran, M. R. Nilsson, A. Clark, Pancreatic beta-cell granule peptides form heteromolecular complexes which inhibit islet amyloid polypeptide fibril formation. *Biochem. J.* **377**, 709–716 (2004).
30. J. C. Hutton, The insulin secretory granule. *Diabetologia* **32**, 271–281 (1989).
31. P. Nedumpully-Govindan, F. Ding, Inhibition of IAPP aggregation by insulin depends on the insulin oligomeric state regulated by zinc ion concentration. *Sci. Rep.* **5**, 8240 (2015).
32. Y. Stefan, P. Meda, M. Neufeld, L. Orci, Stimulation of insulin secretion reveals heterogeneity of pancreatic B cells in vivo. *J. Clin. Invest.* **80**, 175–183 (1987).
33. Z. Ma, G. T. Westermark, K. H. Johnson, T. D. O'Brien, P. Westermark, Quantitative immunohistochemical analysis of islet amyloid polypeptide (IAPP) in normal, impaired glucose tolerant, and diabetic cats. *Amyloid* **5**, 255–261 (1998).
34. K. H. Johnson, T. D. O'Brien, K. Jordan, P. Westermark, Impaired glucose tolerance is associated with increased islet amyloid polypeptide (IAPP) immunoreactivity in pancreatic beta cells. *Am. J. Pathol.* **135**, 245–250 (1989).
35. R. Guardado-Mendoza *et al*., Pancreatic islet amyloidosis, beta-cell apoptosis, and alpha-cell proliferation are determinants of islet remodeling in type-2 diabetic baboons. *Proc. Natl. Acad. Sci. U.S.A.* **106**, 13992–13997 (2009).
36. T. D. O'Brien, A. E. Butler, P. C. Roche, K. H. Johnson, P. C. Butler, Islet amyloid polypeptide in human insulinomas. Evidence for intracellular amyloidogenesis. *Diabetes* **43**, 329–336 (1994).
37. J. F. Paulsson, A. Andersson, P. Westermark, G. T. Westermark, Intracellular amyloid-like deposits contain unprocessed pro-islet amyloid polypeptide (proIAPP) in beta cells of transgenic mice overexpressing the gene for human IAPP and transplanted human islets. *Diabetologia* **49**, 1237–1246 (2006).
38. M. V. C. Cardoso, E. Sabadini, The gelling of κ-carrageenan in light and heavy water. *Carbohydr. Res.* **345**, 2368–2373 (2010).
39. H. Kusumaatmaja, R. Lipowsky, Droplet-induced budding transitions of membranes. *Soft Matter* **7**, 6914–6919 (2011).
40. K. C. Breen, M. Bruce, B. H. Anderton, Beta amyloid precursor protein mediates neuronal cell-cell and cell-surface adhesion. *J. Neurosci. Res.* **28**, 90–100 (1991).
41. L. S. Minamide, A. M. Striegl, J. A. Boyle, P. J. Meberg, J. R. Bamburg, Neurodegenerative stimuli induce persistent ADF/cofilin-actin rods that disrupt distal neurite function. *Nat. Cell Biol.* **2**, 628–636 (2000).